

Nanotextured Spikes of $\alpha\text{-Fe}_2\text{O}_3/\text{NiFe}_2\text{O}_4$ Composite for Efficient Photoelectrochemical Oxidation of Water

Shabeeb Hussain,[†] Mohammad Mahdi Tavakoli,^{‡,§,¶} Aashir Waleed,^{‡,||} Umar Siddique Virk,^{‡,⊥} Shihe Yang,[#] Amir Waseem,[†] Zhiyong Fan,^{*,‡,¶} and Muhammad Arif Nadeem^{*,†,||}

[†]Catalysis and Nanomaterials Lab 27, Department of Chemistry, Quaid-i-Azam University, Islamabad 45320, Pakistan

[‡]Department of Electronic and Computer Engineering, Hong Kong University of Science and Technology, Clear Water Bay, Kowloon, Hong Kong SAR, China

[§]Department of Materials Science and Engineering, Sharif University of Technology, Azadi Street, 113659466 Tehran, Iran

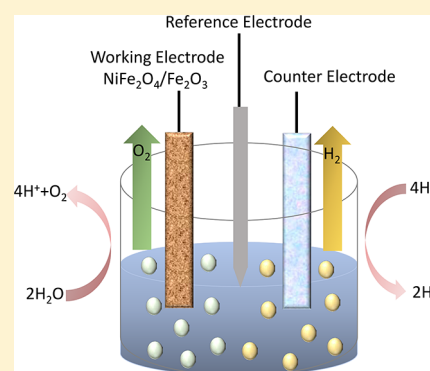
^{||}Department of Electrical Engineering, University of Engineering and Technology, Lahore (FSD Campus), 3.5 km, Khurrianwala-Makuana Bypass, Faisalabad 38000, Pakistan

[⊥]Department of Mechatronics and Control Engineering, University of Engineering and Technology, Lahore (FSD Campus), 3.5 km, Khurrianwala-Makuana Bypass, Faisalabad 38000, Pakistan

[#]Department of Chemistry, William Mong Institute of Nano Science and Technology, The Hong Kong University of Science and Technology, Clear Water Bay, Kowloon, Hong Kong SAR, Hong Kong

Supporting Information

ABSTRACT: We demonstrate for the first time the application of p-NiFe₂O₄/n-Fe₂O₃ composite thin films as anode materials for light-assisted electrolysis of water. The p-NiFe₂O₄/n-Fe₂O₃ composite thin films were deposited on planar fluorinated tin oxide (FTO)-coated glass as well as on 3D array of nanospike (NSP) substrates. The effect of substrate (planar FTO and 3D-NSP) and percentage change of each component (i.e., NiFe₂O₄ and Fe₂O₃) of composite was studied on photoelectrochemical (PEC) water oxidation reaction. This work also includes the performance comparison of p-NiFe₂O₄/n-Fe₂O₃ composite (planar and NSP) devices with pure hematite for PEC water oxidation. Overall, the nanostructured p-NiFe₂O₄/n-Fe₂O₃ device with equal molar 1:1 ratio of NiFe₂O₄ and Fe₂O₃ was found to be highly efficient for PEC water oxidation as compared with pure hematite, 1:2 and 1:3 molar ratios of composite. The photocurrent density of 1:1 composite thin film on planar substrate was equal to 1.07 mA/cm² at 1.23 V_{RHE}, which was 1.7 times higher current density as compared with pure hematite device (0.63 mA/cm² at 1.23 V_{RHE}). The performance of p-NiFe₂O₄/n-Fe₂O₃ composites in PEC water oxidation was further enhanced by their deposition over 3D-NSP substrate. The highest photocurrent density of 2.1 mA/cm² at 1.23 V_{RHE} was obtained for the 1:1 molar ratio p-NiFe₂O₄/n-Fe₂O₃ composite on NSP (NF1-NSP), which was 3.3 times more photocurrent density than pure hematite. The measured applied bias photon-to-current efficiency (ABPE) value of NF1-NSP (0.206%) was found to be 1.87 times higher than that of NF1-P (0.11%) and 4.7 times higher than that of pure hematite deposited on FTO-coated glass (0.044%). The higher PEC water oxidation activity of p-NiFe₂O₄/n-Fe₂O₃ composite thin film as compared with pure hematite is attributed to the Z-path scheme and better separation of electrons and holes. The increased surface area and greater light absorption capabilities of 3D-NSP devices result in further improvement in catalytic activities.



INTRODUCTION

Day-by-day increase in consumption of fossil fuel is causing depletion of crude oil reservoirs and rapid increase in atmospheric carbon dioxide (CO₂). This has dragged the attention of scientists toward green technology, for example, solar energy, which is environmentally friendly and is a clean source of energy. The solar flux irradiating the earth surface (1.3×10^5 TW) exceeds the global energy consumption (1.6×10^1 TW in 2010) by about four orders of magnitude.¹ The conversion of solar energy into a clean form of chemical energy such as hydrogen via photoelectrochemical (PEC) splitting of water could meet the desired target of a cheap and clean source

of energy.^{2,3} Since the first report of successful PEC water splitting by Fujishima and Honda,⁴ various semiconducting materials exhibiting photocatalytic activity have been discovered. In particular, materials with narrow band gap, such as WO₃,⁵ BiVO₄,^{6,7} Fe₂O₃,^{8,9} and NiFe₂O₄¹⁰ are suitable choices for PEC water splitting and are of greater interest. Because of the suitable band gap (2.2 eV), band position, and chemical stability, hematite (Fe₂O₃) is considered to be the most suitable

Received: August 8, 2017

Revised: February 2, 2018

potential candidate to work as photoanode for solar-driven electrolysis.¹¹ Theoretically, a photoconversion efficiency of 16% can be achieved for pure hematite in the conversion process of solar energy to hydrogen via PEC water-splitting reaction.^{12,13} However, practically, maximum photoconversion efficiency of 0.6%¹⁴ has been achieved for pure hematite, which is too low when compared with the theoretical value. It is now well established that this lower solar to hydrogen conversion efficiency of hematite is due to short lifetime of photogenerated charges (<10 ps), short diffusion length of photogenerated holes (2–4 nm), and slow kinetics of water oxidation.^{13,15} Thus efforts were being made to overcome these problems and to enhance the efficiency of hematite photoanode by various methods.^{16–20} Specifically, the strategies adopted for circumventing the above-mentioned drawbacks involve the doping of hematite with the transition metals and appropriate design of nanoarchitecture of hematite particles. These methods altogether increase the light absorption capacity of material,^{21–25} promote the oxygen evolution reaction,^{26–30} and decrease the charge recombination rate.^{31–33} Transition-metal ferrites with the general formula of MFe_2O_4 ($M = Ni, Cu, Zn, Co$) have intriguing properties of narrow band gap and visible-light absorbance with high efficiency.³⁴ MFe_2O_4 has higher conductivity of electric charges due to the hopping process between metal ions of variable oxidation states at O-sites. This property is beneficial for transferring the charge carriers.^{35,36} In addition, MFe_2O_4 has many other advantages such as stability against photocorrosion, low toxicity, low cost, high adsorption ability, and easy preparation.^{37,38}

For the first time, we are reporting the coupling of p- Fe_2O_3 with the n- $NiFe_2O_4$ to address the certain issues associated with hematite, that is, short diffusion length of photogenerated electrons and holes. The conduction band of hematite is more negative as compared with the valence band of nickel ferrite, so the photoexcited electrons in the conduction band of hematite can travel toward the photogenerated holes in the valence band of nickel ferrite. Thus lifetime and diffusion length of electrons and holes increase by this double absorbing mechanism (Scheme 1). During the process, photoexcited electrons from

the conduction band of hematite travel through the outer circuit via valence and conduction bands of nickel ferrite. The p- $NiFe_2O_4/n-Fe_2O_3$ composite thin films were deposited on planar (fluorinated tin oxide (FTO)-coated glass) as well as on perfectly ordered 3D-nanospike (NSP) substrates. The PEC water-splitting studies showed that planar p- $NiFe_2O_4/n-Fe_2O_3$ as well as the 3D-NSP p- $NiFe_2O_4/n-Fe_2O_3$ devices outperformed the pure hematite. Later devices, however, showed a remarkable increase (208%) in photoconversion efficiency compared with hematite device. It is worth mentioning that 3D-NSP devices showed increased PEC activity as compared with planar FTO device and pure hematite device due to the higher surface area and light absorption.⁴⁰ The increased photoconversion efficiencies upon deposition of the composite material on 3D-NSP are essentially due to the diffraction effect because the length, width, and distance between neighboring nanospikes are comparable to the wavelength of visible light.^{39–42} This work also summarizes the PEC water splitting results for two different compositions (1:1 and 1:2 molar ratio) of p- $NiFe_2O_4/n-Fe_2O_3$ composite, of which composite with equal molar ratio (1:1) between $NiFe_2O_4$ and Fe_2O_3 showed the highest activity.

EXPERIMENTAL SECTION

Fabrication of Highly Ordered 3D-NSP Arrays Substrate.

Aluminum foil was cut into pieces of 2.5 cm length and 1.5 cm width and then pressed between two glass slides to flatten the aluminum chips. The chips were sonicated for ~10 min in acetone, isopropanol (IPA), and deionized water, respectively, for removing dirt and impurities on the surface. Aluminum chips were then polished electrochemically in 1:3 v/v solution (perchloric acid in ethanol) by applying DC potential of 12 V for ~2 min at 10 °C.^{43–45} For growing symmetric NSP array, the polished aluminum chips were imprinted by 1×1 cm² homemade silicon mold (consisting of squarely ordered arrays of pillars with 200 nm height and 1200 nm pitch). After that, aluminum chips were anodized under DC voltage of 480 V at 5 °C in the acidic solution (120 mL of 2% aqueous solution of citric acid, 120 mL of ethylene glycol, and 9 mL of 0.1% phosphoric acid) for 6 h. After completion of anodization process the aluminum chips were removed and washed with DI water. For exposing perfectly ordered arrays of NSP, the chips were dipped in the etching solution (1.5% (w/w) of chromic acid and 6% (w/w) of phosphoric acid in water) at 98 °C for 60 min to etch anodized aluminum oxide (AAO). After complete etching of AAO, the exposed 3D nanostructured aluminum chips were rinsed with DI water and dried by compressed air blower. For protection against NaOH solution, a protection layer of Al_2O_3 was grown over nanospikes by low-voltage anodization at 20 V for 2 h in 3.4% aqueous solution of H_2SO_4 . Then, 100 and 50 nm thick layers of Ti and Pt were deposited, respectively, by using magnetron sputtering for more protection against basic electrolyte solution. Finally, a 100 nm-thick FTO was deposited on top of 3D-NSP substrates by using ultrasonic spray pyrolysis (UPS) of ethanolic solution of 0.2 M $SnCl_4$ and 0.04 M of NH_4 . Compressed air was used as a carrier gas for transferring the mist of precursor solution into the decomposition chamber of USP setup. The temperature of the decomposition chamber was maintained at 450 °C.

Deposition of $NiFe_2O_4/Fe_2O_3$ Composite Layer on 3D-NSP Substrate. The USP method was employed for the deposition of photoactive $NiFe_2O_4/Fe_2O_3$ composite thin films on 3D nanostructured multilayered substrate. The calculated amounts of $FeCl_3 \cdot 6H_2O$ and $NiCl_2 \cdot 6H_2O$ in different molar ratios were mixed and dissolved in ethanol. It was followed by the addition of an appropriate amount of acetyl acetone as a complexing agent for making the metallic ion more volatile. A small amount of prepared precursor solution was transferred to the evaporation chamber of USP setup, and the resulting mist was transferred to the decomposition chamber. The temperature in the chamber was kept at 500 °C. Table 1 shows the

Scheme 1. Schematic Representation of Energy Band Positions of $NiFe_2O_4$ and $\alpha-Fe_2O_3$, Dual-Absorbing Mechanism

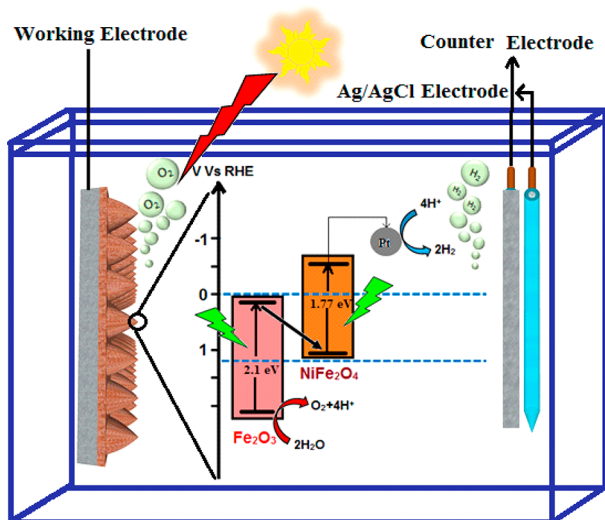
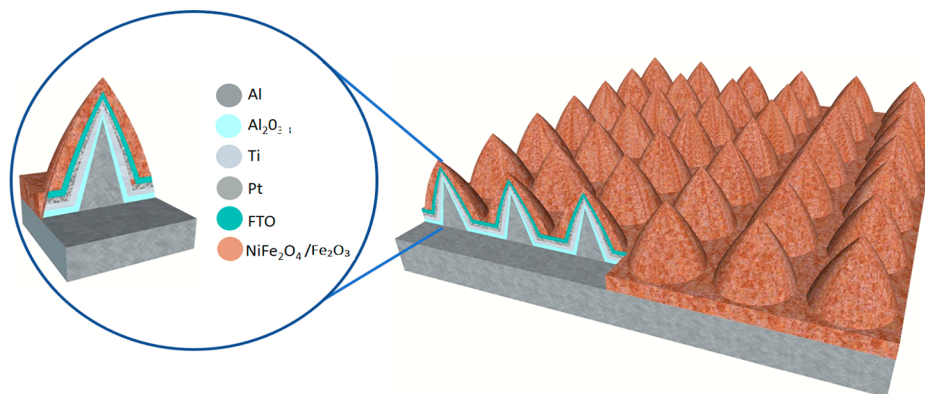


Table 1. Molar Concentrations of the Precursor Solutions Used and Molar Composition Obtained from XRF Analysis

code	molar concentration of $\text{FeCl}_3 \cdot 6\text{H}_2\text{O}$	molar concentration of $\text{NiCl}_2 \cdot 6\text{H}_2\text{O}$	molar composition $\text{Fe}_2\text{O}_3/\text{NiFe}_2\text{O}_4$	
			Fe_2O_3	NiFe_2O_4
NF3	0.05	0.05	1	3
NF2	0.05	0.1	1	2
NF1	0.05	0.15	1	1

Scheme 2. Schematic Description of 3D-NSP Nanostructured Device

molar concentration of the precursor solutions for deposition of $\text{NiFe}_2\text{O}_4/\text{Fe}_2\text{O}_3$ composite layers with different molar ratios of each component. A schematic representation of fabricated 3D-NSP device is shown in Scheme 2.

Deposition of $\text{NiFe}_2\text{O}_4/\text{Fe}_2\text{O}_3$ Composite Layer on Planar FTO-Coated Glass. FTO-coated glass was cut in pieces of 2×2.5 cm dimensions and sonicated for 10 min in isopropyl alcohol (IPA), followed by rinsing with acetone and DI water.^{46–48} Then, one end of cleaned FTO glass was tightly covered by aluminum foil to avoid deposition of metal oxide on this part for wire connection. A similar USP procedure as for 3D-NSP was adopted for deposition of $\text{NiFe}_2\text{O}_4/\text{Fe}_2\text{O}_3$ composite on FTO glass. The same precursor solutions were used for deposition, as mentioned in Table 1.

RESULTS AND DISCUSSION

The structural characterization of fabricated composite thin films was carried out by using powder X-ray diffraction (XRD; Philips PW-1830) with $\text{Cu K}\alpha$ radiation ($\lambda = 1.5406$ Å). The XRD spectra of $\text{NiFe}_2\text{O}_4/\text{Fe}_2\text{O}_3$ composite films on FTO glass are shown in Figure 1. The diffraction patterns reveal that the thin films deposited over FTO-coated glass are of composite type that consists of $\alpha\text{-Fe}_2\text{O}_3$ and NiFe_2O_4 . The diffraction peaks appearing at $2\theta = 30.19, 35.7, 43.45, 57.43,$ and 63.01° are assigned to the 220, 311, 400, 511, and 440 planes of NiFe_2O_4 . This pattern reveals the spinel cubic structure of NiFe_2O_4 .⁴⁹

The relative diffraction peak positions of NiFe_2O_4 are in accordance with previously reported standard diffraction pattern of NiFe_2O_4 (JCPDS no. 01-086-2267), and no extra peak for nickel oxides (NiOx) was present. The diffraction peaks that appeared at $2\theta = 26.5, 33.6, 37.8, 51.5, 54.4, 61.5, 66.6,$ and 78.5° represent FTO peaks corresponding to diffraction planes of 110, 101, 200, 211, 220, 310, 301 and 321, respectively,⁴⁶ while the peaks that appeared at $35.5, 40.9, 49.4, 62.4,$ and 64° in PXRD pattern are ascribed to 110, 113, 024, 214, and 300 reflections planes of hematite, respectively. Peak positions of Fe_2O_3 and FTO are also provided in Figure 1 to distinguish them from the peaks of NiFe_2O_4 . Figure 1 also provides PXRD spectrum for other composite ratios of 1:2 and 1:3. However, it can be clearly visualized that this change in

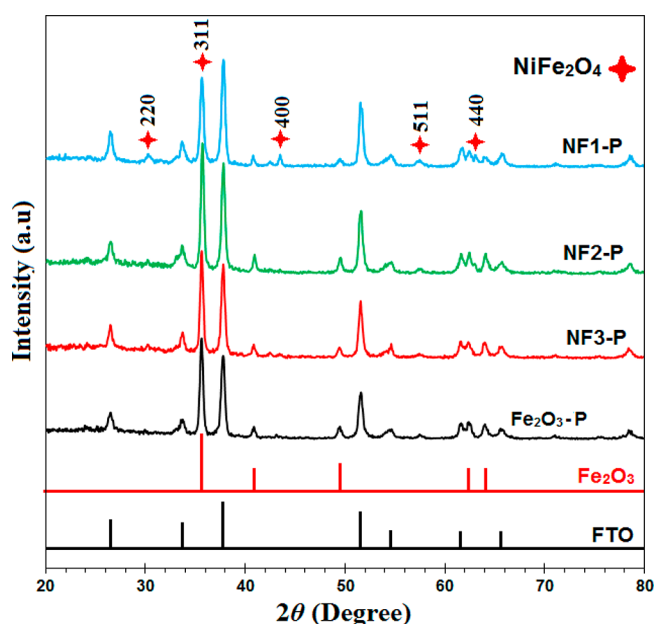


Figure 1. PXRD patterns for different molar ratios of $\text{NiFe}_2\text{O}_4/\alpha\text{-Fe}_2\text{O}_3$ composites on planar FTO substrate and Fe_2O_3 (pure) deposited on FTO-coated glass.

composite ratio does not change the peak locations of composites (NF2 and NF3), and XRD spectra are the same as NF1 composite ratio.

Figure 2 shows the surface composition of $\text{NiFe}_2\text{O}_4/\text{Fe}_2\text{O}_3$ composite thin film by X-ray photoelectronic spectroscopic (XPS) technique. It has been verified by full-scan XPS survey spectrum shown in Figure 2A that Ni, Fe, and O are the main components of the composite thin film. The carbon peak appeared at 285.2 eV is due to the hydrocarbon originating from XPS instrument itself used as a standard.

The high-resolution XPS spectra of Fe 2p are shown in Figure 1B, which shows two splitting peaks at the binding sites of 725 and 711 eV, attributed to Fe ($2p_{1/2}$) and Fe ($2p_{3/2}$),

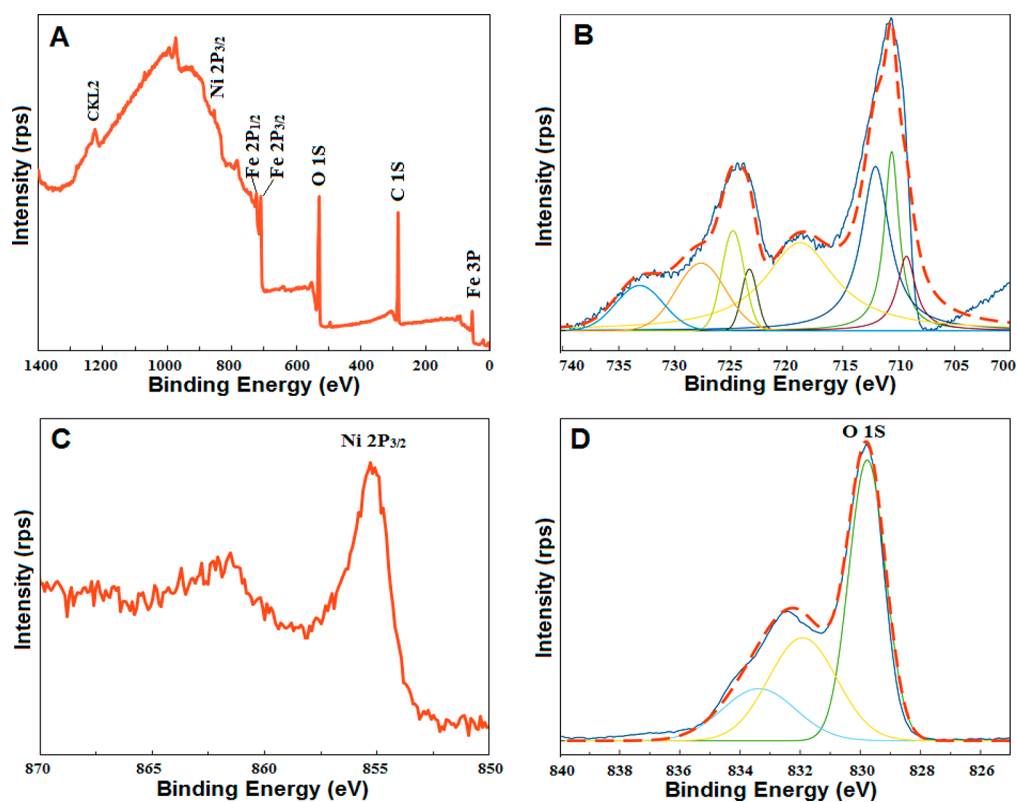


Figure 2. (A) Full-scan XPS spectrum of composite NF1. (B) Fe 2p scan of NF1. (C) Ni 2p scan of NF1. (D) O 1s scan of NF1.

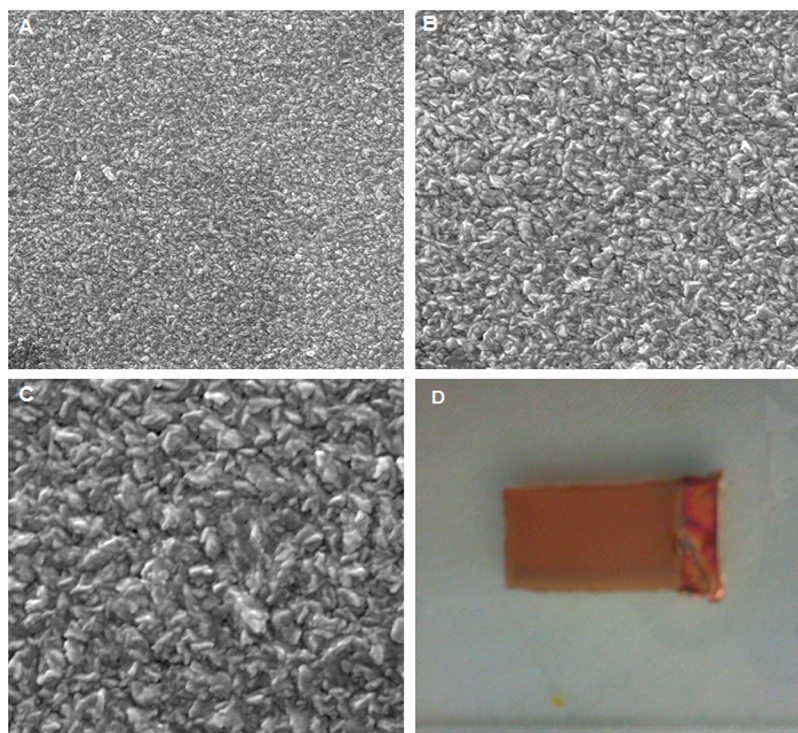


Figure 3. (A) Low-magnification SEM images of $\text{NiFe}_2\text{O}_4/\text{Fe}_2\text{O}_3$ composite thin film on FTO-coated glass (NF1-P). (B,C) High-magnification SEM images of $\text{ZnFe}_2\text{O}_4/\text{Fe}_2\text{O}_3$ thin film on FTO-coated glass (NF1-P). (D) Optical photograph of NF1-P.

respectively. The satellite peak together with Fe ($2\text{P}_{1/2}$) and Fe ($2\text{P}_{3/2}$) indicate that the Fe is present in Fe^{3+} state as a whole. In Figure 2C, the peak at 856 eV represents the Ni $2\text{P}_{3/2}$. The other peak at 862 eV denotes shakeup satellite peak of Ni $2\text{P}_{3/2}$. Furthermore, the high-resolution O 1s spectrum (Figure 2D) is

likely to be fitted into three peaks located at 529.8, 532.3, and 533.8, which are contributed to Ni–Fe–O bonds, substituted hydroxyl group, and physi-/chemisorbed H_2O on the surface. The quantitative elemental analysis of $\text{NiFe}_2\text{O}_4/\alpha\text{-Fe}_2\text{O}_3$ composite thin films was further studied and verified by

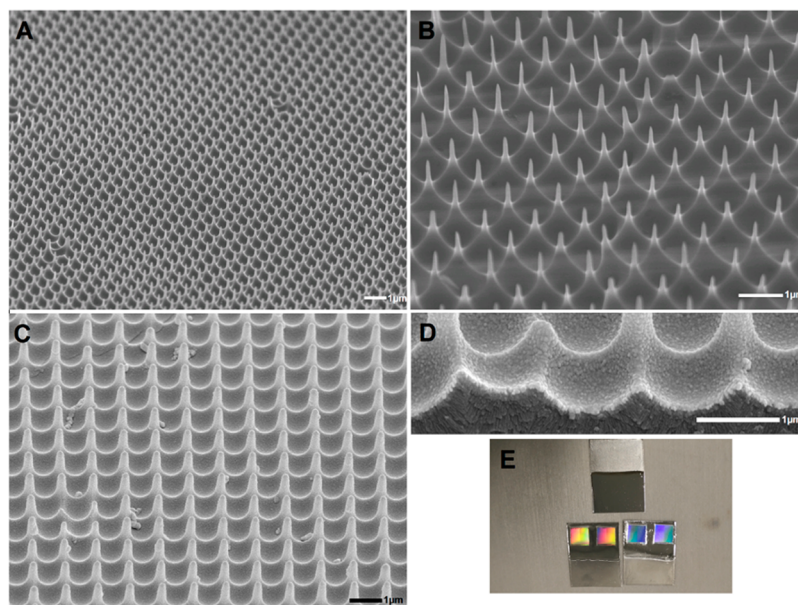


Figure 4. (A,B) Low- and high-magnification SEM image of perfectly ordered 3D-NSP. (C) SEM image of 3D-NSP coated with Ti and Pt protective thin films. (D) Zoomed-in cross-section SEM image of 3D-NSP with protective Ti and Pt thin films deposited on the top of nanospikes. (E) Real image of 3D-NSP substrate before (bottom) and after (top) deposition of protective layers.

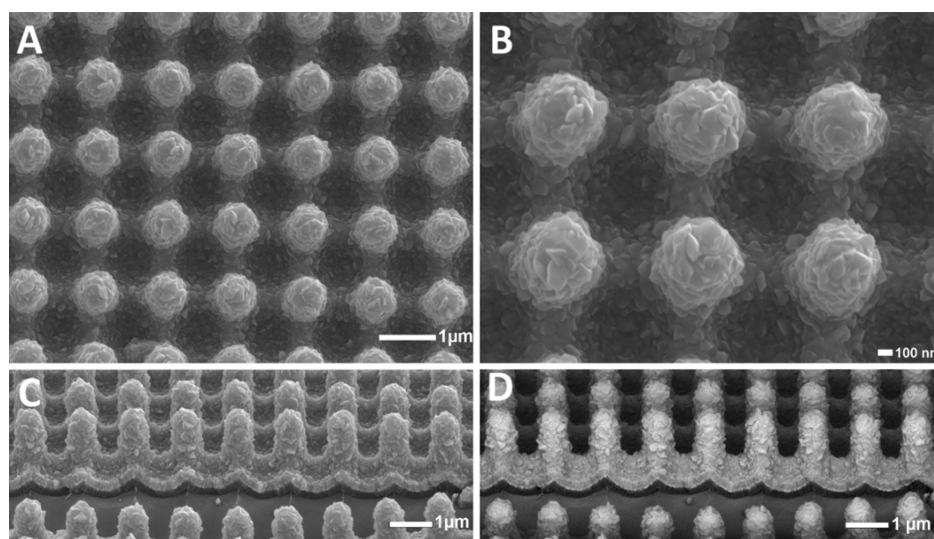


Figure 5. (A) Low- and high-magnification SEM images showing the top view 3D substrate covered with $\text{NiFe}_2\text{O}_4/\text{Fe}_2\text{O}_3$ composite film. (C,D) Cross-sectional SEM image final device.

energy-dispersive X-ray spectrometry (EDS) and X-ray fluorescence (XRF) spectrometry. The results of these tests are summarized in Supporting Information Figure S1.

Surface morphologies of fabricated $\text{NiFe}_2\text{O}_4/\text{Fe}_2\text{O}_3$ composite thin films on planar and 3D-NSP structures were studied by scanning electron microscopy (SEM). Figure 3A–C shows the low- and high-resolution SEM images of $\text{NiFe}_2\text{O}_4/\text{Fe}_2\text{O}_3$ composite thin film deposited on planar FTO-coated glass. It can be clearly observed that FTO has a uniform distribution on top of crystals on its surface.

Figure 4A,B presents the SEM image of as fabricated 3D-NSP substrate at different zoom scales. It is worth noting that the spikes are well-aligned in square fashion with $1.2 \mu\text{m}$ spacing between two adjacent spikes and height of the spikes is 1000 nm. Figure 4C shows the SEM image of 3D-NSP after deposition of protective layers, that is, Ti and Pt. It is quite clear

that protection layers cover the 3D-NSP completely. The two protective film can be easily seen in Figure 4D, showing the cross section of nanospikes. The cross-sectional SEM view of 3D-NSP template with Ti and Pt protective layers on top in Figure 4D is giving a clear evidence that thickness of Ti and Pt layers is 100 and 50 nm, respectively.

The SEM images for top view of final multilayered (after deposition of FTO and $\text{NiFe}_2\text{O}_4/\text{Fe}_2\text{O}_3$ composite) device on 3D-NSP are shown in Figure 5. This verifies that the photoactive $\text{NiFe}_2\text{O}_4/\text{Fe}_2\text{O}_3$ composite is uniformly deposited on 3D template. Figure 5C,D shows the cross-section SEM images of final multilayered device.

The results of elemental mapping by EDS of composite NF1 deposited on FTO-coated glass and 3D template are shown in Figures S2 and S3, respectively. The elemental mapping results

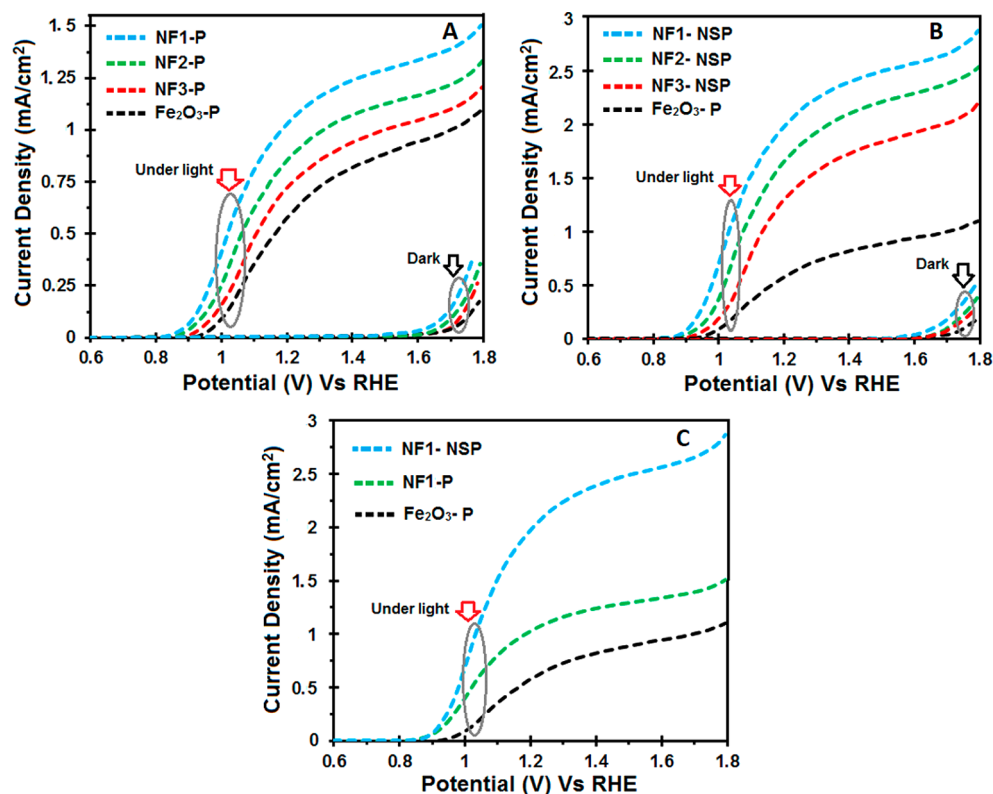


Figure 6. (A) Linear sweep voltammograms (LSV) of $\text{NiFe}_2\text{O}_4/\text{Fe}_2\text{O}_3$ composites deposited on planar FTO-coated glass. (B) LSV curves of $\text{NiFe}_2\text{O}_4/\text{Fe}_2\text{O}_3$ composites deposited on 3D-NSP. (C) Comparison of NF1 photocurrent densities for planar and 3D nanostructure devices with pure hematite.

reveals the homogeneity and perfect layered structure of 3D devices.

After optical characterization of composite thin films on planar and 3D-NSP substrates, light-assisted electrolysis studies for planar and 3D-NSP devices were carried out in 1 M NaOH solution (pH 13.6) using one-compartment three-electrode system. In this three-electrode system, Ag/AgCl was used as reference electrode, platinum coil was used as counter electrode, while the prepared planar or 3D-NSP device was employed as working electrode. For this study, by applying the Nernst equation ($E_{\text{RHE}} = E_{\text{Ag/AgCl}} + 0.059\text{pH} + {}^\circ E_{\text{Ag/AgCl}}$), potential versus Ag/AgCl was converted into the scale of reversible hydrogen electrode (RHE). The linear scan voltammograms (LSVs) of devices were taken between 0.6 to 1.8 V versus RHE with the scan rate of 20 mV/S in dark as well as under illumination of visible light. The visible light was set at 1 sun and was provided by an artificial sunlight simulator (100 mW/cm^2 , AM 1.5G). Figure 6 shows the J - V curve of planar device (A) and 3D-NSP device (B) and a comparison of photocurrent density between planar device and 3D-NSP device (C). Photocurrent densities of all devices were also compared with the pure hematite deposited on FTO-coated glass. Conclusively, it was observed that 3D-NSP $\text{NiFe}_2\text{O}_4/\text{Fe}_2\text{O}_3$ composite thin film devices were most efficient in PEC water oxidation when compared with pure hematite and planar composite devices. It is also worth noting that the activity of water oxidation in PEC cell was the highest for the equal molar (1:1) composite ratio device. The photocurrent density for equal molar planar device NF1-P was calculated as high as 1.07 mA/cm^2 , which is 70% higher than calculated for hematite planar device (Fe_2O_3 -P), that is, 0.63 mA/cm^2 at 1.23 V_{RHE} .

The planar device of NF2-P composite showed 43% increase (0.9 mA/cm^2 at 1.23 V_{RHE}) in photocurrent density as compared with planar bare hematite device deposited on FTO-coated glass (0.63 mA/cm^2). The recorded value of photocurrent density for the device NF3-P was 0.77 mA/cm^2 , which is 22% higher as compared with bare hematite deposited on FTO glass. The higher PEC activities of $\text{NiFe}_2\text{O}_4/\text{Fe}_2\text{O}_3$ composite relative to pure hematite are due to better separation of photoinduced electrons and hole in $\text{NiFe}_2\text{O}_4/\text{Fe}_2\text{O}_3$. The difference between valence and conduction band edges of hematite and NiFe_2O_4 can allow better separation of photo-generated charges. NiFe_2O_4 has a high electrical conductivity due to hopping process between Ni^{2+} and Fe^{3+} , which results in the mediation of electron flow toward the counter electrode of the PEC cell.^{35,36} Because of the better separation of photoinduced charges and high electrical conductivity of $\text{NiFe}_2\text{O}_4/\text{Fe}_2\text{O}_3$ composite, it is more active in PEC water oxidation as compared with pure hematite.

Figure 6B shows the J - V curves of 3D-NSP devices. The recorded value of photocurrent densities for NF3-NSP and NF2-NSP devices at 1.23 V_{RHE} were 1.41 and 1.74 mA/cm^2 , respectively, which are 123.8 and 169.8% higher as compared with pure hematite device on planar FTO glass (0.63 mA/cm^2). An exceptional rise in the photocurrent density (2.1 mA/cm^2) of NF1-NSP at 1.23 V_{RHE} was observed. This high recorded value suggests that the NF1-NSP device is 233% more active as compared with bare hematite device (Fe_2O_3 -P). This outstanding activity is attributed to the increased surface area and higher light trapping tendency of 3D-NSP device.

To further investigate the most active 3D nanostructured device (NF1-NSP) for photoresponse in similar electrolyte

solution, the transient photocurrents were measured at fixed applied voltage (1.23 V vs RHE) via several on–off cycles of irradiation for 30 min. As shown in Figure S5 (see Supporting Information), there is a small decrease in the transient photocurrent density over 30 min of illumination and applied potential of 1.23 V versus RHE, showing that NiFe₂O₄/Fe₂O₃ composite deposited on 3D nanostructured substrates has the ability to withstand in 1 M NaOH solution.

For further elucidating the diagnostic performance of highest active NiFe₂O₄/Fe₂O₃ composite thin films deposited on planar (NF1-P) and 3D-nanostructured substrates (NF1-NSP) relative to pure Fe₂O₃ deposited on FTO glass, we measured applied bias photon-to-current efficiency (ABPE) under illumination provided by solar simulator (100 mW/cm²), according to eq 1 (Figure 7).^{50,51} where j_p is the current density under illumination and $I(\text{light})$ is the intensity of incident light that is equal to 100 mW/cm².

$$\text{ABPE} = \frac{j_p \left(\frac{\text{mA}}{\text{cm}^2} \right) [(1.23 - \text{applied voltage (V)})]}{I(\text{light}) \left(\frac{\text{mW}}{\text{cm}^2} \right)} \times 100$$

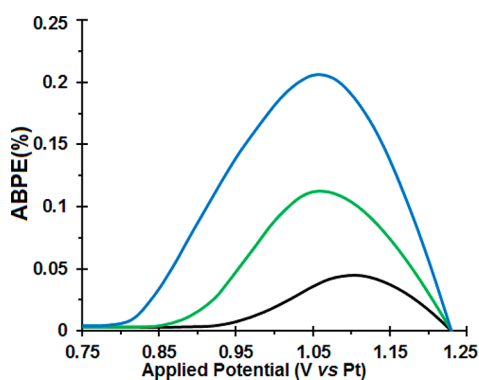


Figure 7. Applied bias photon-to-current efficiency (ABPE, %) as a function of applied potential using two-electrode system (pure hematite deposited on FTO-coated glass (black), NF1-P (green), and NF1-NSP (blue)).

The highest value of ABPE for NF1 deposited on planar substrate (NF1-P) was equal to 0.11%, which is 2.5 times higher value compared with the pure hematite (ABPE) = 0.044%, while the highest value of applied bias photon-to-current-efficiency of NF1 deposited on 3D-nanostructured substrate (NF1-NSP) was 0.206%, which was 1.87 times higher than NF1-P and 4.7 times higher efficiency than pure hematite deposited on FTO-coated glass.

Finally, potentiostatic electrochemical impedance spectroscopy (EIS) measurements were performed for investigation of the origin of enhanced performance of NiFe₂O₄/Fe₂O₃ composite thin films compared with pure hematite. The EIS measurements were performed in 1 M NaOH solution at the applied voltage of 1.23 versus RHE using single-compartment three-electrode system, as previously explained. Figure 8 shows the experimental data for EIS with equivalent Randle circuit (RC). In RC model, R_s represents the solution resistance, R_1 represents the charge-transfer resistance across FTO/semiconductor interface, R_2 is charge-transfer resistance inside semiconductor, and R_3 is assigned as charge-transfer resistance

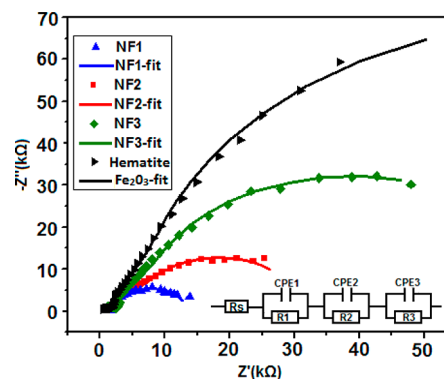


Figure 8. EIS of composite photoanodes with different molar ratio in Nyquist plots in 1 M NaOH at a DC potential of 0.2 V versus Ag/AgCl with an AC potential frequency range from 1 000 000 to 0.1 Hz.

across semiconductor/electrolyte interface because the largest semicircle corresponds to the semiconductor/electrolyte in PEC systems.⁸

The values of charge-transfer resistance (R_3) and double-layered capacitance (CPE_3) are highest for semiconductor/electrolyte interfaces because the most difficult water oxidation reaction takes place at this interface. As shown in Table 2, the

Table 2. Resistance and CPE Values of the Corresponding RC Model

R/K Ω		R1	R2	R3
CPE (μF)	R_s	CPE1	CPE2	CPE3
Fe ₂ O ₃ -P	0.47	1.404	6.224	147.227
ZF3	0.61	2.285×10^{-4}	3.743×10^{-3}	4.184×10^{-3}
ZF2	0.66	2.776×10^{-4}	1.26×10^{-2}	1.7×10^{-2}
ZF1	0.55	3.90×10^{-4}	1.55×10^{-2}	1.88×10^{-2}
		0.942	1.782	13.355
		3.92×10^{-4}	1.68×10^{-2}	2.9×10^{-2}

values of R_3 for p-NiFe₂O₄/α-Fe₂O₃ composites photoanodes are lowered as compared with pure α-Fe₂O₃ photoanode, and the lowest value of resistance is observed for the composite having equal ratio of NiFe₂O₄ and α-Fe₂O₃. There is reduction trend in resistance values across all possible interfaces due to higher charge mobility in NiFe₂O₄/α-Fe₂O₃ composites relative to pure hematite. Thus higher charge mobility of p-NiFe₂O₄/α-Fe₂O₃ composites than α-Fe₂O₃ contributes to its enhanced activities in PEC water splitting.

Overall, this study addresses the two main problems associated with Fe₂O₃, that is, poor photogenerated charge separation and low conductivity. The target has been achieved by coupling p-Fe₂O₃ with n-NiFe₂O₄ because the band positions of hematite align with band position of nickel ferrite in such a way that permits photoexcited electrons to transfer from the conduction band of hematite toward the holes generated in the valence band of nickel ferrite. By this mechanism the photoexcited electrons in hematite can travel directly toward the outer circuit efficiently because the nickel ferrite is a good conductor as compared with hematite. Thus, the holes that were left behind in the valence band of hematite oxidize the water more efficiently in p-Fe₂O₃/n-NiFe₂O₄ composite as compared with bare hematite. The overall results from this PEC study are summarized in Table 3.

Table 3. Summary of the Results Extrapolated from the Photocurrent Density and Photoconversion Efficiency

codes	composition NiFe ₂ O ₄ /Fe ₂ O ₃	photocurrent density (mA/cm ²) at 1.23 V vs RHE
Fe ₂ O ₃ -P	pure hematite	0.63
NF1-P	1:1	1.07
NF2-P	1:2	0.9
NF3-P	1:3	0.77
NF1-NSP	1:1	2.1
NF2-NSP	1:2	1.74
NF3-NSP	1:3	1.41

CONCLUSIONS

NiFe₂O₄/Fe₂O₃ composite thin films were deposited on planar substrate (FTO glass) as well as on perfectly ordered 3D-NSP substrates. The resulting planar and 3D nanostructured devices were used as working electrodes and tested for their activities in PEC water oxidation. The study elucidated that the composite that comprised an equal molar ratio (1:1) of NiFe₂O₄ and Fe₂O₃ showed the highest activity in photoelectrocatalytic water oxidation reaction. Compared with the pure hematite deposited on FTO-coated glass (Fe₂O₃-P), the planar device NF1-P in which the molar ratio between NiFe₂O₄/Fe₂O₃ was adjusted as 1:1 showed ~150% higher photoconversion efficiency at similar applied voltage. The band gap and band positions of Fe₂O₃ and NiFe₂O₄ align in a fashion that permits photoexcited electrons to travel from the conduction band of Fe₂O₃ toward counter electrode via valence and conduction bands of NiFe₂O₄. This phenomenon leads to the better separation of photogenerated electrons and holes and thus the enhanced activity of NiFe₂O₄/Fe₂O₃ composite thin films as compared with pure hematite. The photoconversion efficiencies of NiFe₂O₄/Fe₂O₃ composite films have been further increased by depositing on a substrate that consists of perfectly ordered 3D nanopikes in square manner. The 3D nanostructured device NF1-NSP that has similar photoactive composite thin film like in NF1-P showed 1.87 times higher applied bias photon-to-current-efficiency value than NF1-P device. Electrochemical impedance study verified that charge conductivity of NiFe₂O₄/Fe₂O₃ composite is higher as compared with pure Fe₂O₃. The enhancement of charge conductivity across all possible interfaces is observed in NiFe₂O₄/Fe₂O₃ composites as compared with bare hematite. The increased surface area, better light absorption ability of 3D nanostructured devices, and higher charge conductivity of NiFe₂O₄/Fe₂O₃ composite resulted in the enhanced activity in water oxidation by process of light-assisted electrolysis of water.

ASSOCIATED CONTENT

Supporting Information

The Supporting Information is available free of charge on the ACS Publications website at DOI: 10.1021/acs.langmuir.7b02786.

Figure S1. X-ray spectroscopic results of composite on FTO glass: NF1-P, NF2-P, and NF3-P. Figure S2: Energy-dispersive X-ray spectroscopic images of composite NF1 deposited on FTO-coated glass. Figure S3: Elemental mapping by energy-dispersive X-ray spectroscopy of composite NF-1 deposited on 3D template. Figure S4: XRF results of composite NF1-P, NF2-P, and NF3-P. Figure S5: Photocurrent density versus time

plotted for NF1-NSP in 1 M NaOH electrolyte under light provided by artificial sunlight simulator. (PDF)

AUTHOR INFORMATION

Corresponding Authors

*M.A.N.: E-mail: manadeem@qau.edu.pk. Tel:+92-51-9064-2062.

*Z.F.: E-mail: eezfan@ust.hk.

ORCID

Mohammad Mahdi Tavakoli: 0000-0002-8393-6028

Aashir Waleed: 0000-0002-6929-8373

Zhiyong Fan: 0000-0002-5397-0129

Muhammad Arif Nadeem: 0000-0003-0738-9349

Notes

The authors declare no competing financial interest.

ACKNOWLEDGMENTS

This work is supported by Higher Education Commission (HEC) of Pakistan (no. 20-2704/NRPU/R&D/HEC/12 and project no. 6172). S. H. acknowledges the IRSIP scholarship of Higher Education Commission (HEC) of Pakistan for financial support while carrying out the research work in the Hong Kong University of Science and Technology.

REFERENCES

- (1) Hisatomi, T.; Kubota, J.; Domen, K. Recent advances in semiconductors for photocatalytic and photoelectrochemical water splitting. *Chem. Soc. Rev.* **2014**, *43*, 7520–7535.
- (2) Gratzel, M. Photoelectrochemical cells. *Nature* **2001**, *414*, 338–344.
- (3) Rioult, M.; Magnan, H.; Stanesco, D.; Barbier, A. Single Crystalline Hematite Films for Solar Water Splitting: Ti-Doping and Thickness Effects. *J. Phys. Chem. C* **2014**, *118*, 3007–3014.
- (4) Fujishima, A.; Honda, K. Electrochemical Photolysis of Water at a Semiconductor Electrode. *Nature* **1972**, *238*, 37–38.
- (5) Bär, M.; Weinhardt, L.; Marsen, B.; Cole, B.; Gaillard, N.; Miller, E.; Heske, C. Mo incorporation in WO₃ thin film photoanodes: Tailoring the electronic structure for photoelectrochemical hydrogen production. *Appl. Phys. Lett.* **2010**, *96*, 032107.
- (6) Jia, Q.; Iwashina, K.; Kudo, A. Facile fabrication of an efficient BiVO₄ thin film electrode for water splitting under visible light irradiation. *Proc. Natl. Acad. Sci. U. S. A.* **2012**, *109*, 11564–11569.
- (7) Berglund, S. P.; Flaherty, D. W.; Hahn, N. T.; Bard, A. J.; Mullins, C. B. Photoelectrochemical Oxidation of Water Using Nanostructured BiVO₄ Films. *J. Phys. Chem. C* **2011**, *115*, 3794–3802.
- (8) Tahir, A. A.; Wijayantha, K. G. U.; Saremi-Yarahmadi, S.; Mazhar, M.; McKee, V. Nanostructured α -Fe₂O₃ Thin Films for Photoelectrochemical Hydrogen Generation. *Chem. Mater.* **2009**, *21*, 3763–3772.
- (9) Pendlebury, S. R.; Cowan, A. J.; Barroso, M.; Sivula, K.; Ye, J.; Gratzel, M.; Klug, D. R.; Tang, J.; Durrant, J. R. Correlating long-lived photogenerated hole populations with photocurrent densities in hematite water oxidation photoanodes. *Energy Environ. Sci.* **2012**, *5*, 6304–6312.
- (10) Liu, G.; Wang, K.; Gao, X.; He, D.; Li, J. Fabrication of mesoporous NiFe₂O₄ nanorods as efficient oxygen evolution catalyst for water splitting. *Electrochim. Acta* **2016**, *211*, 871–878.
- (11) Wang, G.; Ling, Y.; Wheeler, D. A.; George, K. E. N.; Horsley, K.; Heske, C.; Zhang, J. Z.; Li, Y. Facile Synthesis of Highly Photoactive α -Fe₂O₃-Based Films for Water Oxidation. *Nano Lett.* **2011**, *11*, 3503–3509.
- (12) Sivula, K.; Le Formal, F.; Gratzel, M. Solar Water Splitting: Progress using Hematite (α -Fe₂O₃) Photoelectrodes. *ChemSusChem* **2011**, *4*, 432–449.

- (13) Wang, G.; Ling, Y.; Wheeler, D. A.; George, K. E.; Horsley, K.; Heske, C.; Zhang, J. Z.; Li, Y. Facile Synthesis of Highly Photoactive α -Fe₂O₃-based Films for Water Oxidation. *Nano Lett.* **2011**, *11*, 3503–3509.
- (14) Kim, J. Y.; Magesh, G.; Youn, D. H.; Jang, J. W.; Kubota, J.; Domen, K.; Lee, J. S. Single-crystalline, Wormlike Hematite Photoanodes for Efficient Solar Water Splitting. *Sci. Rep.* **2013**, *3*, 2681.
- (15) Gurudayal; Chiam, S. Y.; Kumar, M. H.; Bassi, P. S.; Seng, H. L.; Barber, J.; Wong, L. H. Improving the Efficiency of Hematite Nanorods for Photoelectrochemical Water Splitting by Doping with Manganese. *ACS Appl. Mater. Interfaces* **2014**, *6* (8), 5852–5859.
- (16) Emery, J. D.; Schlepütz, C. M.; Guo, P.; Riha, S. C.; Chang, R. P. H.; Martinson, A. B. F. Atomic Layer Deposition of Metastable β -Fe₂O₃ via Isomorphic Epitaxy for Photoassisted Water Oxidation. *ACS Appl. Mater. Interfaces* **2014**, *6*, 21894–21900.
- (17) Fu, L.; Yu, H.; Zhang, C.; Shao, Z.; Yi, B. Cobalt Phosphate Group Modified Hematite Nanorod Array as Photoanode for Efficient Solar Water Splitting. *Electrochim. Acta* **2014**, *136*, 363–369.
- (18) Liu, J.; Liang, C.; Xu, G.; Tian, Z.; Shao, G.; Zhang, L. Ge-doped Hematite Nanosheets with Tunable Doping Level, Structure and Improved Photoelectrochemical Performance. *Nano Energy* **2013**, *2*, 328–336.
- (19) Luan, P.; Xie, M.; Fu, X.; Qu, Y.; Sun, X.; Jing, L. Improved Photoactivity of TiO₂-Fe₂O₃ Nanocomposites for Visible-Light Water Splitting after Phosphate Bridging and its Mechanism. *Phys. Chem. Chem. Phys.* **2015**, *17*, 5043–5050.
- (20) Liu, J.; Cai, Y. Y.; Tian, Z. F.; Ruan, G. S.; Ye, Y. X.; Liang, C. H.; Shao, G. S. Highly Oriented Ge-Doped Hematite Nanosheet Arrays for Photoelectrochemical Water Oxidation. *Nano Energy* **2014**, *9*, 282–290.
- (21) Riha, S. C.; Klahr, B. M.; Tyo, E. C.; Seifert, S.; Vajda, S.; Pellin, M. J.; Hamann, T. W.; Martinson, A. B. F. Atomic Layer Deposition of a Submonolayer Catalyst for the Enhanced Photoelectrochemical Performance of Water Oxidation with Hematite. *ACS Nano* **2013**, *7*, 2396–2405.
- (22) Ling, Y.; Wang, G.; Wheeler, D. A.; Zhang, J. Z.; Li, Y. Sn-Doped Hematite Nanostructures for Photoelectrochemical Water Splitting. *Nano Lett.* **2011**, *11*, 2119–2125.
- (23) Hsu, Y.-P.; Lee, S.-W.; Chang, J.-K.; Tseng, C.-J.; Lee, K.-R.; Wang, C.-H. Effects of Platinum Doping on the Photoelectrochemical Properties of Fe₂O₃ Electrodes. *Int. J. Electrochem. Sci.* **2013**, *8*, 11615.
- (24) Tallarida, M.; Das, C.; Cibrev, D.; Kukli, K.; Tamm, A.; Ritala, M.; Lana-Villarreal, T.; Gómez, R.; Leskelä, M.; Schmeisser, D. Modification of Hematite Electronic Properties with Trimethyl Aluminum to Enhance the Efficiency of Photoelectrodes. *J. Phys. Chem. Lett.* **2014**, *5*, 3582–3587.
- (25) Shen, S.; Jiang, J.; Guo, P.; Kronawitter, C. X.; Mao, S. S.; Guo, L. Effect of Cr Doping on the Photoelectrochemical Performance of Hematite Nanorod Photoanodes. *Nano Energy* **2012**, *1*, 732–741.
- (26) Cowan, A. J.; Barnett, C. J.; Pendlebury, S. R.; Barroso, M.; Sivula, K.; Grätzel, M.; Durrant, J. R.; Klug, D. R. Activation Energies for the Rate-Limiting Step in Water Photooxidation by Nanostructured α -Fe₂O₃ and TiO₂. *J. Am. Chem. Soc.* **2011**, *133*, 10134–10140.
- (27) Mirbagheri, N.; Wang, D.; Peng, C.; Wang, J.; Huang, Q.; Fan, C.; Ferapontova, E. E. Visible Light Driven Photoelectrochemical Water Oxidation by Zn- and Ti-Doped Hematite Nanostructures. *ACS Catal.* **2014**, *4*, 2006–2015.
- (28) Wheeler, D. A.; Wang, G.; Ling, Y.; Li, Y.; Zhang, J. Z. Nanostructured Hematite: Synthesis, Characterization, Charge Carrier Dynamics, and Photoelectrochemical Properties. *Energy Environ. Sci.* **2012**, *5*, 6682–6702.
- (29) Du, C.; Yang, X.; Mayer, M. T.; Hoyt, H.; Xie, J.; McMahon, G.; Bischofing, G.; Wang, D. Hematite-Based Water Splitting with Low Turn-On Voltages. *Angew. Chem., Int. Ed.* **2013**, *52*, 12692–12695.
- (30) Qiu, Y.; Leung, S.-F.; Zhang, Q.; Hua, B.; Lin, Q.; Wei, Z.; Tsui, K.-H.; Zhang, Y.; Yang, S.; Fan, Z. Efficient Photoelectrochemical Water Splitting with Ultrathin Films of Hematite on Three dimensional Nanophotonic Structures. *Nano Lett.* **2014**, *14*, 2123–2129.
- (31) Sivula, K.; Le Formal, F.; Grätzel, M. Solar Water Splitting: Progress Using Hematite (α -Fe₂O₃) Photoelectrodes. *ChemSusChem* **2011**, *4*, 432–449.
- (32) Cesar, I.; Sivula, K.; Kay, A.; Zboril, R.; Grätzel, M. Influence of Feature Size, Film Thickness, and Silicon Doping on the Performance of Nanostructured Hematite Photoanodes for Solar Water Splitting. *J. Phys. Chem. C* **2009**, *113*, 772–782.
- (33) Park, S.; Kim, D.; Lee, C.; Seo, S.-D.; Kim, H.; Han, H.; Hong, K.; Kim, D.-W. Surface-Area-Tuned, Quantum-Dot-Sensitized Heterostructured Nanoarchitectures for Highly Efficient Photoelectrodes. *Nano Res.* **2014**, *7*, 144–153.
- (34) Harish, K. N.; Bhojya Naik, H. S.; Prashanth Kumar, P. N.; Viswanath, R. Optical and Photocatalytic Properties of Solar Light Active Nd-Substituted Ni Ferrite Catalysts: For Environmental Protection. *ACS Sustainable Chem. Eng.* **2013**, *1*, 1143–1153.
- (35) Neburchilov, V.; Wang, H.; Martin, J. J.; Qu, W. A review on air cathodes for zinc air fuel cells. *J. Power Sources* **2010**, *195*, 1271–1291.
- (36) Zhu, H.; Zhang, S.; Huang, Y. X.; Wu, L.; Sun, S. Monodisperse M(x)Fe(3-x)O₄ (M = Fe, Cu, Co, Mn) nanoparticles and their electrocatalysis for oxygen reduction reaction. *Nano Lett.* **2013**, *13*, 2947–2951.
- (37) Cui, B.; Lin, H.; Li, J.-B.; Li, X.; Yang, J.; Tao, J. Ring Structured NiCo₂O₄ Nanoplatelets: Synthesis, Characterization, and Electrocatalytic Applications. *Adv. Funct. Mater.* **2008**, *18*, 1440–1447.
- (38) Scaife, D. E. Oxide semiconductors in photoelectrochemical conversion of solar energy. *Sol. Energy* **1980**, *25*, 41–54.
- (39) Li, J.; Qiu, Y.; Wei, Z.; Lin, Q.; Zhang, Q.; Yan, K.; Chen, H.; Xiao, S.; Fan, Z.; Yang, S. A three-dimensional hexagonal fluorine-doped tin oxide nanocone array: a superior light harvesting electrode for high performance photoelectrochemical water splitting. *Energy Environ. Sci.* **2014**, *7*, 3651–3658.
- (40) Leung, S.-F.; Gu, L.; Zhang, Q.; Tsui, K.-H.; Shieh, J.-M.; Shen, C.-H.; Hsiao, T.-H.; Hsu, C.-H.; Lu, L.; Li, D.; Lin, Q.; Fan, Z. Roll-to-roll fabrication of large scale and regular arrays of three-dimensional nanopikes for high efficiency and flexible photovoltaics. *Sci. Rep.* **2015**, *4*, 4243.
- (41) Hussain, S.; Hussain, S.; Waleed, A.; Tavakoli, M. M.; Wang, Z.; Yang, S.; Fan, Z.; Nadeem, M. A. Fabrication of CuFe₂O₄/ α -Fe₂O₃ Composite Thin Films on FTO Coated Glass and 3-D Nanospire Structures for Efficient Photoelectrochemical Water Splitting. *ACS Appl. Mater. Interfaces* **2016**, *8* (51), 35315–35322.
- (42) Hussain, S.; Hussain, S.; Waleed, A.; Tavakoli, M. M.; Yang, S.; Rauf, M. K.; Fan, Z.; Nadeem, M. A. Spray Pyrolysis Deposition of ZnFe₂O₄/Fe₂O₃ Composite Thin Films on Hierarchical 3-D Nanospikes for Efficient Photoelectrochemical Oxidation of Water. *J. Phys. Chem. C* **2017**, *121*, 18360–18368.
- (43) Waleed, A.; Tavakoli, M. M.; Gu, L.; Wang, Z.; Zhang, D.; Manikandan, A.; Zhang, Q.; Zhang, R.; Chueh, Y.-L.; Fan, Z. Lead-Free Perovskite Nanowire Array Photodetectors with Drastically Improved Stability in Nanoengineering Templates. *Nano Lett.* **2017**, *17* (1), 523–530.
- (44) Waleed, A.; Fan, Z. Fabrication of stable organometallic halide perovskite NWs based optoelectronic devices. *Sci. Bull.* **2017**, *62* (9), 645–647.
- (45) Tavakoli, M. M.; Waleed, A.; Gu, L.; Zhang, D.; Tavakoli, R.; Lei, B.; Su, W.; Fang, F.; Fan, Z. A non-catalytic vapor growth regime for organohalide perovskite nanowires using anodic aluminum oxide templates. *Nanoscale* **2017**, *9* (18), 5828–5834.
- (46) Waleed, A.; Zhang, Q.; Tavakoli, M. M.; Leung, S.; Gu, L.; He, J.; Mo, X.; Fan, Z. Performance improvement of solution-processed CdS/CdTe solar cells with a thin compact TiO₂ buffer layer. *Science Bulletin* **2016**, *61* (1), 86–91.
- (47) Tavakoli, M. M.; Tavakoli, R.; Nourbakhsh, Z.; Waleed, A.; Virk, U. S.; Fan, Z. High Efficiency and Stable Perovskite Solar Cell Using ZnO/rGO QDs as an Electron Transfer Layer. *Adv. Mater. Interfaces* **2016**, *3* (9), 1500790.

(48) Waleed, A.; Tavakoli, M. M.; Gu, L.; Hussain, S.; Zhang, D.; Poddar, S.; Wang, Z.; Zhang, R.; Fan, Z. All Inorganic Cesium Lead Iodide Perovskite Nanowires with Stabilized Cubic Phase at Room Temperature and Nanowire Array-Based Photodetectors. *Nano Lett.* **2017**, *17*, 4951.

(49) Dixit, G.; Singh, J. P.; Srivastava, R. C.; Agrawal, H. M.; Choudhary, R. J.; Gupta, A. Structural and magnetic behavior of NiFe₂O₄ thin film grown by pulsed laser deposition. *Indian J. Pure Appl. Phys.* **2010**, *48*, 287–291.

(50) Varadhan, P.; Fu, H.-C.; Priante, D.; Retamal, J. R. D.; Zhao, C.; Ebaid, M.; Ng, T. K.; Ajia, I.; Mitra, S.; Roqan, I. S.; Ooi, B. S.; He, J.-H. Surface Passivation of GaN Nanowires for Enhanced Photoelectrochemical Water-Splitting. *Nano Lett.* **2017**, *17*, 1520.

(51) Ebaid, M.; Kang, J. H.; Lim, S. H.; Cho, Y. H.; Ryu, S. W. *RSC Adv.* **2015**, *5*, 23303–23310.